

4D Radar-Inertial Odometry based on Gaussian Modeling and Multi-Hypothesis Scan Matching

Fernando Amodeo¹, Luis Merino, *Member, IEEE*¹ and Fernando Caballero¹

Abstract—4D millimeter-wave (mmWave) radars are sensors that provide robustness against adverse weather conditions (rain, snow, fog, etc.), and as such they are increasingly used for odometry and SLAM (Simultaneous Location and Mapping). However, the noisy and sparse nature of the returned scan data proves to be a challenging obstacle for existing registration algorithms, especially those originally intended for more accurate sensors such as LiDAR. Following the success of 3D Gaussian Splatting for vision, in this paper we propose a summarized representation for radar scenes based on global simultaneous optimization of 3D Gaussians as opposed to voxel-based approaches, and leveraging its inherent Probability Density Function (PDF) for registration. Moreover, we propose tackling the problem of radar noise entirely within the scan matching process by optimizing multiple registration hypotheses for better protection against local optima of the PDF. Finally, following existing practice we implement an Extended Kalman Filter-based Radar-Inertial Odometry pipeline in order to evaluate the effectiveness of our system. Experiments using publicly available 4D radar datasets show that our Gaussian approach is comparable to existing registration algorithms, outperforming them in several sequences.

Our code and results can be publicly accessed at: <https://github.com/robotics-upo/gaussian-rio-cpp>

I. INTRODUCTION

4D millimeter-wave (mmWave) radars have earned considerable popularity in the world of robotics as an alternative to classic camera or LiDAR sensors due to their robustness against adverse weather conditions (rain, snow, fog, etc.), as well as their compact size and low power consumption. As such, there is considerable interest in incorporating these sensors in odometry and SLAM applications. A key component of such system is the modeling and scan matching algorithm. Point clouds are used to capture the geometry of the scene at a given time, and subsequent scans are compared (matched) to the reference model in order to extract localization information. Popular established algorithms that perform this task include the Normal Distributions Transform (NDT) [1] or Generalized Iterative Closest Point (GICP) [2]. However, despite working well for LiDAR [3–5], radar point clouds are considerably more challenging to register because they are sparser, noisier, and have a narrower field of view; and, as a result, these algorithms often struggle with the geometry of certain scenes.

We introduce a new method for modeling and registering 4D radar point clouds using 3D Gaussians. Following the success of 3D Gaussian Splatting (3DGS) for vision [6], we propose the use of a collection of 3D Gaussians for modeling

the geometry of a scene. As in [6] (and in contrast to NDT [1]), we simultaneously optimize all parameters of the model, including the position, scaling, rotation and correspondences between points and Gaussians. This approach is entirely featureless, and does not require any priors other than an initial set of centroids. Moreover, we propose a registration step that considers multiple simultaneous hypotheses in order to add further robustness against radar noise. Finally, we integrate our algorithms into a Radar-Inertial Odometry (RIO) pipeline using an Extended Kalman Filter (EKF) (see Fig. 1), which we then use to evaluate our Gaussian methods against several established registration algorithms on multiple datasets and radar types.

This paper is organized as follows: Section II reviews existing related literature, Sections III and IV describe the proposed Gaussian modeling and scan matching components respectively, Section V describes the EKF-based RIO pipeline used in the experiments; Section VI shows experimental results, and Section VII concludes the paper proposing future work.

II. RELATED WORK

Registration of incoming point clouds with respect to previous ones is a key technique used in 3D LiDAR and 4D radar odometry and SLAM systems [3–5] [7–12]. In particular, the most widely used algorithm for aligning point clouds is Generalized Iterative Closest Point (GICP) [2]. This algorithm calculates a distribution probability at each point based on its neighborhood, and optimizes a distribution-to-distribution scan matching function. In the case of radar scans, this is a more difficult task compared to LiDAR because of the lower number and density of points, as well as higher measurement noise/uncertainty in each point’s position. For this reason [9] proposed the Adaptive Probability Distribution variant of the algorithm (APDGICP), which leverages GICP’s ability to make use of the spatial probability distribution of each point, calculating the required point position covariance matrices according to the radar specifications. However, this is still in essence an approach focused on individual points, without attempting to extract larger scale geometric features that may be more stable and robust for registration purposes.

The Normal Distributions Transform (NDT) algorithm [1] subdivides a point cloud using a voxel grid and computes normal distributions for each cell that contains points. Scan matching is performed by maximizing the resulting Probability Density Function (PDF) with respect to an incoming scan. An important limitation of this algorithm is that the grid

¹Service Robotics Laboratory – Universidad Pablo de Olavide (Seville), Spain {famousur, lmercab, fcaballero}@upo.es

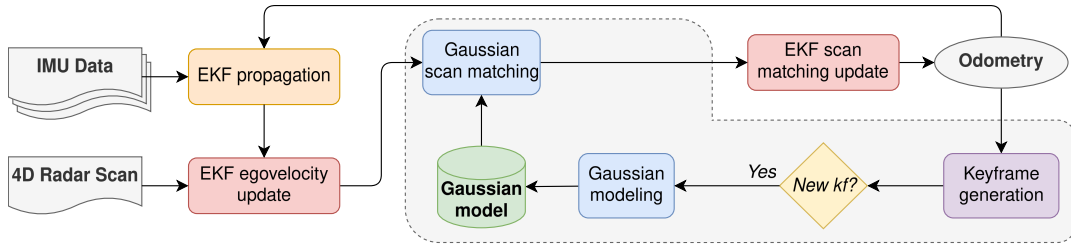


Fig. 1. Overview of the Radar-Inertial Odometry pipeline including our proposed Gaussian modeling and scan matching processes. Bold font indicates input/output, the highlighted area indicates our contribution

structure itself imposes restrictions on the geometry, and the resulting model may not be fine grained enough to accurately model the geometry of the environment. Another problem lies in that discontinuities in the probability function are produced when partially registered points cross cell boundaries during optimization. NDT has been used with radar scans too [13] [14]. Voxelized GICP (VGICP) [15] is a derivative that combines NDT’s voxel-based representation with the distribution-to-distribution based approach of GICP for registration. G3Reg [16] is another derivative of NDT, which performs classification on each voxel (plane/cluster/point) in order to merge plane cells together, and extract semantic information to further aid scan matching. In all these algorithms, each individual Gaussian is modeled separately using their associated subcloud extracted from the segmentation. However, we are interested in approaches that jointly optimize all Gaussians, looking at the entire point cloud.

3D Gaussian Splatting (3DGS) [6] is a popular technique for creating a model of a scene from multiple posed images. A 3DGS model is a collection of multiple 3D normal distributions (Gaussians) freely distributed in space, each also containing color/radiance information encoded using spherical harmonics. Even though this technique was originally developed as an alternative to Neural Radiance Fields (NeRF) [17] for novel view synthesis, researchers have successfully leveraged this representation to develop SLAM solutions [18–20]. Visual-LiDAR methods that improve the robustness of 3DGS with priors sourced from LiDAR input have also been developed [21–23]. However, 3DGS and these works are all designed for visual input, and they cannot be easily reworked to fully replace it with other sensors such as LiDAR or radar due to the nature of the representation. This affects the rendering process in particular: while NeRF’s ray casting framework can be easily adapted to directly predict the output of a Signed Distance Field (SDF) [24] (therefore removing the volume rendering component from the system), the differentiable tile rasterizer is a core part of 3DGS that cannot be avoided, neither during training nor inference; thus requiring significant redesign efforts in order to synthesize other types of data such as LiDAR scans [25].

Following 3DGS as inspiration, we define a purely geometric Gaussian modeling algorithm for radar point clouds based on simultaneous optimization of 3D Gaussians. This representation fundamentally differs from NDT in the fact

that Gaussians are not bound to a predefined voxel grid, and all parameters of the model are jointly optimized instead of subdividing the clouds and individually generating a Gaussian for each subcloud.

III. GAUSSIAN MODELING

Given a point cloud \mathcal{P} containing M points $\{\mathbf{p}_i | i = 0, 1, \dots, M\}$ with $\mathbf{p}_i \in \mathbb{R}^3$, our goal is creating a summarized representation of its geometry for use with downstream tasks such as mapping or localization. We model the geometry of a given radar scene using normal distributions, as in [1] [6] [15] [16].

A. Parametrization

We parametrize the Gaussian model \mathcal{G} of a scene as a collection of N independent trivariate normal distributions (**3D Gaussians**), each modeling the geometry of an individual region in space. The model is described by the following parameters of each Gaussian $\theta_j = \{\boldsymbol{\mu}_j, \mathbf{s}_j, \mathbf{q}_j\}$:

- Center point $\boldsymbol{\mu}_j \in \mathbb{R}^3$, indicating the mean of the distribution.
- Scaling vector $\mathbf{s}_j \in \mathbb{R}^3$, indicating the standard deviations in each dimension. We impose a minimum size restriction so that Gaussians do not become infinitely small (and Mahalanobis distances infinitely large).
- Rotation quaternion $\mathbf{q}_j \in \mathbb{H}$, compactly encoding the orientation of the Gaussian. In order to ensure that the quaternions remain unitary during the optimization, we normalize them prior to usage.

Unlike Gaussian Mixture Models (GMMs), we do not define π_j weight parameters for the prior probability of a point being generated by a given Gaussian. This is because point cloud data does not encode a complete population of points – it merely represents a *sample* of said population, biased by factors such as the physical geometric properties of the sensor. For instance, sampling density is inversely proportional to distance from the sensor. This means we cannot model these prior probabilities, and as such we only consider posterior probabilities after a point is assigned to a Gaussian (using e.g. the shortest Euclidean distance).

The scaling and rotation parameters succinctly describe the covariance matrix of a normal distribution [26] [27]. We first derive a rotation matrix $\mathbf{R}_j = \mathbf{R}\{\mathbf{q}_j\}$, and a scaling matrix $\mathbf{S}_j = \text{diag}(\exp_{\circ}(\mathbf{s}_j))$, where $\exp_{\circ}(\mathbf{x})$ is element-wise natural exponentiation and $\mathbf{R}\{\mathbf{q}\}$ is the rotation

matrix derived from a given quaternion. We then define a matrix $\mathbf{M}_j = \mathbf{R}_j \mathbf{S}_j$ that maps a mean-centered point into the Gaussian's correlation space, and finally derive the covariance matrix $\Sigma_j = \mathbf{M}_j \mathbf{M}_j^T$ of the distribution.

B. Initialization

First, it is necessary to determine N , that is, the number of 3D Gaussians in the model. We propose choosing N proportionally based on the number of points, so that richer scans can be represented with more Gaussians. The proportion should also consider the sparsity of the point clouds generated by the radar used. The model \mathcal{G} is then initialized with all \mathbf{s}_j set to 0 (indicating unit scale), and all \mathbf{q}_j set to the unit quaternion. As for $\boldsymbol{\mu}_j$, we perform Bisecting K-Means clustering to find initial estimates for the centers of the Gaussians.

C. Optimization

\mathcal{G} is optimized iteratively using gradient descent. Each epoch involves the following steps:

- Each point of \mathcal{P} is matched to the nearest Gaussian center point $\boldsymbol{\mu}_j$. This process builds a set G_j for each Gaussian, containing all matched points. We use the standard Euclidean distance in this step as opposed to the Mahalanobis distance in order to avoid a feedback loop between center and covariance matrix optimization that results in exploding gradients.
- Each point \mathbf{p}_i is transformed to the coordinate space of its assigned Gaussian as such: $\hat{\mathbf{p}}_i = \mathbf{M}_j^{-1}(\mathbf{p}_i - \boldsymbol{\mu}_j)$. Note that $\mathbf{M}_j^{-1} = \mathbf{S}_j^{-1} \mathbf{R}_j^T$, and \mathbf{S}_j^{-1} is trivial to calculate since \mathbf{S}_j is a diagonal matrix.
- The parameters of \mathcal{G} (in other words, all θ_j) are updated using the gradient of the loss function.

We define the following loss function for each θ_j , derived from the log PDF of the multivariate normal distribution:

$$\mathcal{L}_j = \frac{1}{2|G_j|} \sum_{\mathbf{p}_i \in G_j} \hat{\mathbf{p}}_i^T \hat{\mathbf{p}}_i + \sum_k^3 \mathbf{s}_{jk}. \quad (1)$$

The loss function \mathcal{L} of the entire model \mathcal{G} can be obtained by taking the mean of the loss values across all Gaussians.

IV. GAUSSIAN MULTI-HYPOTHESIS SCAN MATCHING

Given a Gaussian model \mathcal{G} and a point cloud \mathcal{P} , we define a registration process that estimates the pose of the robot ξ with respect to \mathcal{G} . The algorithm is based on the simultaneous optimization of multiple hypotheses centered around the current predicted position of the robot, in order to increase the robustness against local optima. At the end of the optimization, the hypotheses are judged against a scoring function, and the best hypothesis is selected as the output of the scan matching algorithm while the other hypotheses are discarded. Note that this is unlike a classical particle filter, which does persist the hypotheses throughout time.

A. Definitions

We define the robot pose ξ to be a member of $SE(3)$; that is, it includes a translational component $\mathbf{t} \in \mathbb{R}^3$ and rotational component $\mathbf{q} \in SO(3)$, with respect to *some* frame of reference. We consider that the uncertainty about the true robot pose follows *some* probability distribution: $\xi \sim P$. Given a suitable model of P , we can randomly sample a swarm of K pose particles $\hat{\xi}^k$, each representing a different hypothesis, and use an optimization algorithm that evaluates each particle against \mathcal{G} to further refine these estimates until one of the particles reaches a suitable optimum. We believe exploring the solution space using a particle swarm increases robustness in challenging situations, especially when dealing with large rotations or translations.

B. Optimization

The process is performed iteratively using Gauss-Newton. Each iteration involves the following steps:

- We define K virtual copies of \mathcal{P} called \mathcal{P}^k , each registered according to every pose hypothesis $\hat{\xi}^k$.
- Every point \mathbf{p}_i^k of \mathcal{P}^k is matched to the Gaussian θ_j in \mathcal{G} that results in the lowest Mahalanobis distance, which we call d_i^k .
- We perform the usual Gauss-Newton update step for each particle $\hat{\xi}^k$, using the sums of squared Mahalanobis distances as the function to optimize, as in GICP. We also exclude points whose d_i^k is greater than a given distance threshold d_{\max} .

The optimization stops when all particles converge to a solution (i.e. when the update applied is under a given order of magnitude), or when a maximum number of iterations is reached; whichever happens first. The resulting output pose of the registration algorithm is the particle with the lowest value of the scoring function \mathcal{L}_k defined as follows:

$$\mathcal{L}_k = \frac{1}{M} \sum_i^M \min(d_i^k, d_{\max}), \quad (2)$$

where M is the number of points in the scan. We consider a failure condition when the output particle has not converged.

C. Keyframing

A common technique used in odometry systems is keyframing. Certain poses of the robot are selected to become local reference points (keyframes) that are typically used for registration, pose graph optimization or (in the case of SLAM) loop closure purposes. In our case, we only use keyframing to select individual radar point clouds to undergo Gaussian modeling, and serve as reference for Gaussian scan matching of subsequent radar point clouds. The system only retains the pose and Gaussian model of the most recently generated keyframe. This approach, compared to trivial successive applications of the scan matching algorithm, has the benefit of reducing the accumulated error, though it also means the criteria used to select keyframe candidates needs to be carefully designed to generate an appropriate keyframe pacing. We use a simple set of criteria to decide when a new

pose ξ^j qualifies to become a new keyframe. Given the most recent keyframe ξ^i , we can derive the $SE(3)$ transformation relative to the keyframe $T = \xi^j \ominus \xi^i = \{\mathbf{t}, \mathbf{q}\}$. The criteria are then simply that any of the following must hold:

- For the translational component: $\|\mathbf{t}\|_2 \geq t_{\max}$, where t_{\max} is the maximum translation threshold.
- For the rotational component: $2 \cos^{-1} |q_w| \geq \alpha_{\max}$, where α_{\max} is the maximum rotation threshold.

As a fallback, if no scans have returned a successful match during the past given time interval t , a keyframe is automatically generated.

V. INERTIAL ODOMETRY WITH EKF

In order to evaluate the suitability and effectiveness of the Gaussian algorithms for Radar-Inertial Odometry, it is necessary to define a pipeline for use in the experiments. Following well established practice [12] [28] [29], we use an Extended Kalman Filter in our odometry solution to tightly integrate all incoming sensor information: inertial data, radar egovelocity observations, and scan matching results. In order to simplify the formulation, we only use Error State filtering for rotational variables, as opposed to the entire state. We employ the right-handed North-West-Up (NWU) convention typical of robotics, and consider three reference frames: world (w), body/IMU (b) and radar (r). The rotation matrix \mathbf{C}_f^g transforms a vector from frame f to frame g , likewise $\mathbf{C}_g^f = (\mathbf{C}_f^g)^T$. We decompose each \mathbf{C} into an error part and a nominal quaternion part as follows: $\mathbf{C} = \exp([\delta\boldsymbol{\theta}]_{\times}) \mathbf{R}\{\mathbf{q}\}$, approximating the error part as $\mathbf{I} + [\delta\boldsymbol{\theta}]_{\times}$ for the purposes of linearization.

The state (\mathbf{x}), control (\mathbf{u}) and noise (\mathbf{w}) vectors of the filter are the following:

$$\mathbf{x} = \begin{bmatrix} \mathbf{p} \\ \mathbf{v} \\ \mathbf{t}_r^b \\ \mathbf{b}_a \\ \mathbf{b}_\omega \\ \delta\boldsymbol{\theta}_b^w \\ \delta\boldsymbol{\theta}_r^b \end{bmatrix}; \mathbf{u} = \begin{bmatrix} \mathbf{a} \\ \boldsymbol{\omega} \end{bmatrix}; \mathbf{w} = \begin{bmatrix} \mathbf{w}_v \\ \mathbf{w}_\theta \\ \mathbf{w}_a \\ \mathbf{w}_\omega \\ \mathbf{w}_{b_a} \\ \mathbf{w}_{b_\omega} \end{bmatrix}, \quad (3)$$

where \mathbf{p} is the position, \mathbf{v} is the velocity, \mathbf{t}_r^b is the translation between radar and IMU, \mathbf{b}_a and \mathbf{b}_ω are the accelerometer/gyroscope biases, each $\delta\boldsymbol{\theta}$ is the error part of its corresponding \mathbf{C} frame expressed as a tangential rotation $\in \mathfrak{so}(3)$, and \mathbf{a} and $\boldsymbol{\omega}$ are the IMU accelerometer/gyroscope readings. The position and velocity of the robot are expressed in the world frame, while the nominal rotations \mathbf{q}_b^w and \mathbf{q}_r^b are stored outside the filter state as quaternions. Velocity and attitude process noise are modeled by \mathbf{w}_v and \mathbf{w}_θ respectively. We follow Kalibr's IMU noise model [30]¹, and consider both additive (\mathbf{w}_a , \mathbf{w}_ω) and random walk noise (\mathbf{w}_{b_a} , \mathbf{w}_{b_ω}) in accelerometer/gyroscope readings.

There also exists a vector $\mathbf{g} = -[0 \ 0 \ 9.80511]^T$ modeling the Earth's gravity treated as a constant, as we do not

consider long enough travel distances for changes in the plane tangent to the Earth's surface to matter.

A. EKF initialization

First, we initialize all components of the state vector \mathbf{x} to 0, and the rotational variables to the unit quaternion. The initial radar-to-IMU frame (\mathbf{t}_r^b , \mathbf{q}_r^b) can be supplied externally. The robot is assumed to remain still during the first few seconds, which allows for averaging initial accelerometer/gyroscope readings and extracting an estimate of the body-frame gravity vector $\tilde{\mathbf{g}}_b$ (after flipping sign) and the gyroscope bias \mathbf{b}_ω respectively. An initial value for the roll/pitch components of \mathbf{q}_b^w can then be derived from $\tilde{\mathbf{g}}_b$, while the yaw component is set to 0 since we are not incorporating a compass/magnetometer. In addition, we derive the initial accelerometer bias as $\mathbf{b}_a = \mathbf{C}_b^w (\mathbf{C}_b^w \tilde{\mathbf{g}}_b - \mathbf{g})$, thus taking into account the difference in magnitude between the expected and observed gravity vectors.

We initialize the covariance matrix mostly as 0, except for the subblocks related to \mathbf{t}_r^b , \mathbf{b}_a , \mathbf{b}_ω , $\delta\boldsymbol{\theta}_b^w$ and $\delta\boldsymbol{\theta}_r^b$, whose diagonals we fill in according to supplied initial values.

B. EKF propagation

We use a simplified inertial strapdown formulation that assumes movement to be linear instead of being perturbed by the current angular velocity reading of the gyroscope, due to the short time interval and small change in attitude (in effect equivalent to first order integration):

$$\mathbf{p} \leftarrow \mathbf{p} + \mathbf{v}t + \frac{1}{2}(\mathbf{C}_b^w(\mathbf{a} - \mathbf{b}_a) + \mathbf{g})t^2, \quad (4)$$

$$\mathbf{v} \leftarrow \mathbf{v} + (\mathbf{C}_b^w(\mathbf{a} - \mathbf{b}_a) + \mathbf{g})t, \quad (5)$$

$$\mathbf{q} \leftarrow \mathbf{q} \otimes \exp\left(\frac{1}{2}(\boldsymbol{\omega} - \mathbf{b}_\omega)t\right). \quad (6)$$

The strapdown formulation is linearized in order to propagate the covariance matrix:

$$\mathbf{P} \leftarrow \mathbf{F}\mathbf{P}\mathbf{F}^T + \mathbf{N}\mathbf{Q}\mathbf{N}^T, \quad (7)$$

where \mathbf{F} is the linearized state transition matrix, \mathbf{Q} is the noise covariance matrix, and \mathbf{N} is the noise state transition matrix. These three matrices are sparsely populated: $\mathbf{F} = \mathbf{I}$ and $\mathbf{Q} = \mathbf{N} = \mathbf{0}$, except for the following subblocks:

$$\mathbf{F}_{p v} = \mathbf{I}t; \mathbf{F}_{p b_a} = -\frac{1}{2}\mathbf{C}_b^w t^2; \mathbf{F}_{p \delta\boldsymbol{\theta}_b^w} = -\frac{1}{2}[\mathbf{C}_b^w \mathbf{a}]_{\times} t^2; \quad (8)$$

$$\mathbf{F}_{v b_a} = \mathbf{F}_{\delta\boldsymbol{\theta}_b^w b_\omega} = -\mathbf{C}_b^w t; \mathbf{F}_{v \delta\boldsymbol{\theta}_b^w} = -[\mathbf{C}_b^w \mathbf{a}]_{\times} t; \quad (9)$$

$$\mathbf{Q}_{v v} = \mathbf{I}\sigma_v^2; \mathbf{Q}_{\theta \theta} = \mathbf{I}\sigma_\theta^2; \mathbf{Q}_{a a} = \mathbf{I}\frac{\sigma_a^2}{t}; \quad (10)$$

$$\mathbf{Q}_{\omega \omega} = \mathbf{I}\frac{\sigma_\omega^2}{t}; \mathbf{Q}_{b_a b_a} = \mathbf{I}\sigma_{b_a}^2 t; \mathbf{Q}_{b_\omega b_\omega} = \mathbf{I}\sigma_{b_\omega}^2 t; \quad (11)$$

$$\mathbf{N}_{p a} = \frac{1}{2}\mathbf{C}_b^w t^2; \mathbf{N}_{v a} = \mathbf{N}_{\delta\boldsymbol{\theta}_b^w \omega} = \mathbf{C}_b^w t; \quad (12)$$

$$\mathbf{N}_{v v} = \mathbf{N}_{\delta\boldsymbol{\theta}_b^w \theta} = \mathbf{N}_{b_a b_a} = \mathbf{N}_{b_\omega b_\omega} = \mathbf{I}, \quad (13)$$

where σ_v , σ_θ , σ_a , σ_ω , σ_{b_a} and σ_{b_ω} are the standard deviations of the respective components of \mathbf{w} .

¹<https://github.com/ethz-asl/kalibr/wiki/IMU-Noise-Model>

C. EKF update and error state reset

Given observation \mathbf{y} , residual observation vector \mathbf{r} , observation covariance matrix \mathbf{R} and linearized observation matrix \mathbf{H} (so that $\mathbf{r} \approx \mathbf{y} - \mathbf{H}\mathbf{x}$), we can proceed to apply the Kalman filter equations (in Joseph form):

$$\mathbf{K} = \mathbf{P}\mathbf{H}^T(\mathbf{H}\mathbf{P}\mathbf{H}^T + \mathbf{R})^{-1}; \mathbf{L} = \mathbf{I} - \mathbf{K}\mathbf{H}, \quad (14)$$

$$\mathbf{x} \leftarrow \mathbf{x} + \mathbf{K}\mathbf{r}; \mathbf{P} \leftarrow \mathbf{L}\mathbf{P}\mathbf{L}^T + \mathbf{K}\mathbf{R}\mathbf{K}^T. \quad (15)$$

As previously mentioned, rotations are expressed as error state in the EKF, and after an EKF update the nominal value of each $\delta\boldsymbol{\theta}$ becomes non-zero, making it necessary to incorporate the estimated error back into the state as follows:

$$\mathbf{q} \leftarrow \delta\mathbf{q} \otimes \mathbf{q}; \delta\mathbf{q} = \exp\left(\frac{1}{2}\delta\boldsymbol{\theta}\right), \quad (16)$$

$$\delta\boldsymbol{\theta} \leftarrow 0; \mathbf{P} \leftarrow \mathbf{G}\mathbf{P}\mathbf{G}^T; \mathbf{G}_{\delta\theta\delta\theta} = \mathbf{R}\{\delta\mathbf{q}\}, \quad (17)$$

where \mathbf{G} is the error reset matrix, and it is a sparse matrix equal to \mathbf{I} except for every $\delta\theta\delta\theta$ subblock.

Finally, in order to prevent especially noisy observations from causing instability in the filter, we follow [29] and perform Mahalanobis outlier rejection, using a threshold calculated from a given percentile of the χ^2 distribution.

D. Radar egovelocit observation

Following previous works, we directly observe the robot's velocity by leveraging the Doppler effect in measurements returned by the radar. We use the RANSAC-LSQ algorithm [29] to both filter out outlier (dynamic) points, and estimate the current radar-frame velocity of the robot, including a covariance matrix. The filtered point cloud is then fed to the Gaussian modeling and scan matching algorithm in the following subsection. The observation model used to perform the EKF update is as follows:

$$\mathbf{r} = \mathbf{y} - \mathbf{C}_b^r([\boldsymbol{\omega}]_{\times}\mathbf{t}_r^b + \mathbf{C}_w^b\mathbf{v}); \quad (18)$$

$$\mathbf{H}_{:v} = \mathbf{C}_b^r\mathbf{C}_w^b; \mathbf{H}_{:t_r^b} = \mathbf{C}_b^r[\boldsymbol{\omega}]_{\times}; \mathbf{H}_{:b_w} = \mathbf{C}_b^r[\mathbf{t}_r^b]_{\times}; \quad (19)$$

$$\mathbf{H}_{:\delta\theta_w^v} = \mathbf{C}_b^r\mathbf{C}_w^b[\mathbf{v}]_{\times}; \mathbf{H}_{:\delta\theta_b^v} = \mathbf{C}_b^r([\boldsymbol{\omega}]_{\times}\mathbf{t}_r^b + \mathbf{C}_w^b\mathbf{v})_{\times}. \quad (20)$$

E. Scan matching observation

The Gaussian modeling and scan matching algorithms allow us to observe robot poses relative to previous keyframes. In other words, given a keyframe pose ξ^k we can observe the change in translation and rotation that has occurred since said keyframe. We randomly initialize the pose particle swarm with a distribution $\mathbf{P} \sim \mathcal{N}(\xi^x, \boldsymbol{\Sigma})$ where ξ^x is the relative robot pose formed from the current nominal state of the EKF: $\xi^x = \{\mathbf{p}, \mathbf{q}\} \ominus \xi^k$, and $\boldsymbol{\Sigma}$ is a covariance matrix indicating the desired dispersion of the particles for each of the 6 degrees of freedom (X/Y/Z/roll/pitch/yaw). Afterwards, we apply the scan matching algorithm and obtain a single optimized observation pose ξ^y , from which a residual pose can be obtained: $\xi^r = \xi^y \ominus \xi^x = \{\delta\mathbf{p}, \delta\mathbf{q}\}$. Since the attitude error quaternion $\delta\mathbf{q}$ can be approximated as $\delta\mathbf{q} = \exp(\frac{1}{2}\delta\boldsymbol{\theta}) \approx [1 \frac{1}{2}\delta\boldsymbol{\theta}^T]^T$ for very small errors, the attitude error vector can be approximated as $\delta\boldsymbol{\theta} \approx \frac{2}{\delta q_w}\delta\mathbf{q}_w$. This

allows us to construct the residual vector $\mathbf{r} = [\delta\mathbf{p}^T \delta\boldsymbol{\theta}^T]^T$ to be fed to the EKF update equation – note that this vector contains X/Y/Z/roll/pitch/yaw components (in this order). The non-zero subblocks of the observation matrix \mathbf{H} can be defined as such: $\mathbf{H}_{\delta p p} = \mathbf{H}_{\delta\theta\delta\theta} = \mathbf{C}_w^k$, where k corresponds to the keyframe's reference frame. We currently use a fixed observation covariance matrix \mathbf{R} , although we believe it is possible to leverage the optimized particle swarm returned by the scan matching algorithm to estimate this matrix.

Furthermore, we follow [31] and constrain the observation model described above by removing degrees of freedom that are deemed noisy in the scan matching due to the properties of the sensor. For example, radars have lower resolution in the Z axis, which degrades the usefulness of Z/roll/pitch information returned by scan matching algorithms. In order to ignore the unreliable degrees of freedom, we transform the residual vector, observation matrix and covariance matrix by removing the rows and/or columns corresponding to Z/roll/pitch prior to applying the EKF update.

VI. EXPERIMENTAL RESULTS

We use existing public 4D radar datasets for evaluation. In particular, we selected the NTU4DRadLM [8] and Snail-Radar [32] datasets, because together they cover multiple radar types (Oculii Eagle and ARS548), multiple robot platform types (handcart and car), and adverse conditions.

We evaluate relative translation/rotation errors using the modern and flexible `evo` evaluation package [33], while preserving existing practice by using a custom evaluation script that follows the behavior of older packages such as `rpg_trajectory_evaluation` as closely as possible. In the case of Snail-Radar sequences, we report rotation errors in mrad/m instead of °/m due to much smaller errors.

Besides our Gaussian methods, we evaluate four ablations within our RIO framework: one without multi-hypothesis registration, and three using common established scan matching algorithms (NDT, GICP and VGICP) directly with radar point clouds. We use the current nominal state of the EKF directly as the initial estimate for single-hypothesis scan matching. The NDT version uses the implementation provided by the well known PCL (Point Cloud Library), while the GICP and VGICP versions use `small_gicp` [34] as the underlying implementation. In the case of Oculii Eagle scans, we set a target of 20 points per Gaussian; while for ARS548 scans, due to the much lower number of returned points, we set a target of 8 points per Gaussian. In both cases we sample a swarm of 8 particles during scan matching, which we believe are enough for testing purposes without significantly increasing processing times. Other parameters include $t_{\max} = 15\text{m}$ and $\alpha_{\max} = 5^\circ$ for keyframing, $d_{\max} = 4$ for scan matching, and $0.5\text{m}/2^\circ$ for multi-hypothesis particle dispersion. These parameters were chosen to suit the typical depth range/sparsity relation of a radar.

The source code of our system, which includes the Gaussian algorithms and the odometry pipeline, can be accessed online on GitHub². We include the script used to generate

²<https://github.com/robotics-upo/gaussian-rio-cpp>

TABLE I

RESULTS ON NTU4DRadLM DATASET (OCULII EAGLE). BEST RESULTS IN **BOLD**, SECOND BEST RESULTS UNDERLINED. METHODS MARKED WITH * ARE SELF-REPORTED METRICS. EV: EGOVELOCITY, SM: SCAN MATCHING, ABL.: ABLATION. RELATIVE TRANSLATION ERRORS (t_{rel}) ARE EXPRESSED IN %, RELATIVE ROTATION ERRORS (r_{rel}) IN $^{\circ}$ /M, AND TIME IN MS

| Radar/Method | Inputs | | | | cp | | nyl | | loop2 | | loop3 | |
|------------------------------------|--------|----|----|-------------|-------------|---------------|-------------|---------------|-------------|---------------|-------------|---------------|
| Oculii Eagle | IMU | EV | SM | Time | t_{rel} | r_{rel} | t_{rel} | r_{rel} | t_{rel} | r_{rel} | t_{rel} | r_{rel} |
| NTU4DRadLM Baseline: GICP* [8] | – | ✓ | ✓ | – | 4.13 | 0.0552 | 4.62 | 0.0184 | 4.84 | 0.0060 | 3.22 | 0.0060 |
| NTU4DRadLM Baseline: Fast-LIO* [8] | – | – | ✓ | – | 2.94 | 0.0468 | 3.80 | 0.0208 | 7.16 | 0.0057 | 4.55 | 0.0064 |
| 4DRadarSLAM: APDGICP* [9] | – | ✓ | ✓ | – | 3.56 | 0.0369 | 3.55 | 0.0171 | 6.09 | 0.0082 | 4.09 | 0.0097 |
| EFEAR-4D* [10] | – | ✓ | ✓ | – | 5.09 | 0.0125 | 8.93 | 0.0166 | 37.27 | 0.0152 | 37.01 | 0.0175 |
| RIV-SLAM* [11] | ✓ | ✓ | ✓ | – | 2.58 | 0.0342 | – | – | 2.69 | 0.0456 | – | – |
| EKF-RIO [29] | ✓ | ✓ | – | – | 14.76 | 0.3955 | 35.89 | 0.2464 | 44.31 | 0.0349 | 50.23 | 0.0910 |
| (Abl.) NDT Scan Matching [1] | ✓ | ✓ | ✓ | 12.61 | 2.42 | 0.0345 | 7.80 | 0.0408 | 5.61 | 0.0065 | 7.84 | 0.0100 |
| (Abl.) GICP Scan Matching [2] | ✓ | ✓ | ✓ | 12.33 | 2.93 | 0.0428 | 2.97 | 0.0111 | 2.99 | 0.0038 | <u>3.50</u> | <u>0.0042</u> |
| (Abl.) VGICP Scan Matching [15] | ✓ | ✓ | ✓ | 6.79 | 2.43 | 0.0362 | 2.56 | 0.0136 | 2.73 | <u>0.0036</u> | 3.84 | 0.0047 |
| (Abl.) Gaussian Single Hypothesis | ✓ | ✓ | ✓ | 5.29 | <u>2.15</u> | 0.0318 | <u>2.46</u> | <u>0.0116</u> | 2.44 | 0.0030 | 3.97 | 0.0043 |
| Gaussian Multi-Hypothesis | ✓ | ✓ | ✓ | 19.17 | 1.64 | <u>0.0310</u> | 2.41 | 0.0117 | <u>2.61</u> | <u>0.0036</u> | 3.71 | 0.0040 |

TABLE II

RESULTS ON SNAIL-RADAR DATASET (OCULII EAGLE AND ARS548). BEST RESULTS IN **BOLD**, SECOND BEST RESULTS UNDERLINED. RELATIVE TRANSLATION ERRORS (t_{rel}) ARE EXPRESSED IN % AND RELATIVE ROTATION ERRORS (r_{rel}) IN MRAD/M

| Radar/Method | st_20231213_1 | | iaf_20231213_2 | | iaf_20231213_3 | | if_20231213_4 | | if_20231213_5 | |
|-----------------------------------|---------------|---------------|----------------|---------------|----------------|---------------|---------------|---------------|---------------|---------------|
| Oculii Eagle | t_{rel} | r_{rel} | t_{rel} | r_{rel} | t_{rel} | r_{rel} | t_{rel} | r_{rel} | t_{rel} | r_{rel} |
| (Abl.) NDT Scan Matching [1] | 4.13 | 0.5286 | 2.04 | 0.0519 | 3.95 | 0.0653 | 2.86 | 0.0786 | 3.15 | 0.0771 |
| (Abl.) GICP Scan Matching [2] | 3.77 | 0.5118 | 2.93 | 0.0629 | 4.05 | 0.0629 | 2.77 | 0.1136 | 4.58 | 0.1572 |
| (Abl.) VGICP Scan Matching [15] | 3.68 | <u>0.5141</u> | 3.06 | 0.0610 | 3.17 | 0.0551 | 2.53 | 0.1167 | 4.44 | 0.1489 |
| (Abl.) Gaussian Single Hypothesis | <u>3.36</u> | 0.5204 | 2.85 | 0.0689 | 2.84 | <u>0.0537</u> | 2.36 | <u>0.0927</u> | <u>4.00</u> | <u>0.1457</u> |
| Gaussian Multi-Hypothesis | 3.33 | 0.5147 | <u>2.45</u> | <u>0.0543</u> | <u>2.89</u> | 0.0498 | <u>2.55</u> | 0.1093 | 4.32 | 0.1569 |
| ARS548 | t_{rel} | r_{rel} | t_{rel} | r_{rel} | t_{rel} | r_{rel} | t_{rel} | r_{rel} | t_{rel} | r_{rel} |
| (Abl.) GICP Scan Matching [2] | 1.69 | 0.3049 | 3.36 | 0.0507 | 3.29 | 0.0487 | 2.42 | 0.0761 | 2.26 | 0.0796 |
| (Abl.) VGICP Scan Matching [15] | 1.95 | 0.2798 | <u>2.57</u> | <u>0.0494</u> | <u>3.10</u> | <u>0.0491</u> | 2.81 | <u>0.0777</u> | 2.12 | 0.0836 |
| (Abl.) Gaussian Single Hypothesis | 1.34 | 0.3727 | 2.50 | 0.0487 | 2.77 | 0.0475 | <u>2.47</u> | 0.0826 | 2.37 | 0.0740 |
| Gaussian Multi-Hypothesis | <u>1.60</u> | 0.3573 | 4.02 | 0.0756 | 6.80 | 0.1000 | 2.93 | 0.0894 | <u>2.25</u> | <u>0.0746</u> |

the odometry trajectories, and the script used to evaluate trajectories with `evo`. The code also contains all details regarding the system parameters we used, such as EKF covariance initialization, IMU/noise parameters, etc.

A. Results on NTU4DRadLM

We evaluate using the NTU4DRadLM dataset [8], which includes scans captured by an Oculii Eagle radar, and a VectorNav VN-100 IMU. Besides the evaluation performed with our pipeline, we also include previously published results of several radar-focused odometry methods, in order to provide context on the current performance of the state of the art. Due to a lack of Radar-Inertial methods, we also include radar-only methods. These include the GICP and Fast-LIO baselines tested in the original NTU4DRadLM paper, the APDGICP algorithm tested in the follow-up 4DRadarSLAM paper [9], as well as other works such as EFEAR-4D [10] or RIV-SLAM [11]. All works are categorized according to the sensory input used (IMU, egoveLOCITY, scan matching). We include self-reported metrics as-is, as the trajectory files needed for metric calculation are usually not made public. The results for EKF-RIO [29] are generated by running the system directly, as there are no published results on this dataset. We report metrics without loop closure whenever possible, in order to focus on evaluating pure odometry.

We evaluate the `cp`, `nyl` (low speed handcart), `loop2` and `loop3` (high speed car) sequences. The `garden` and `loop1` sequences are excluded because they contain large gaps in the IMU and radar data, respectively.

Table I shows the comparison between all methods. Our Gaussian methods provide the best or second best results for all sequences except for `loop3`, which seems to favor

GICP-based methods (both baseline and our implementation). Moreover, in 3 out of the 4 sequences the multi-hypothesis scan matching approach provides improvements in translation error, especially in `cp`.

Additionally, we report the average scan matching processing time for each method running under our odometry pipeline. The evaluation platform is a desktop PC equipped with an Intel Core i9-9900X CPU and 128 GB of RAM. The single-hypothesis version of our method achieves the fastest scan matching processing times, closely followed by VGICP. The multi-hypothesis approach, despite simultaneously registering 8 particles at once, is only 3.62x slower than the single-hypothesis version. We also mention that our current RIO implementation is entirely sequential, and that Gaussian modeling at keyframes consumes up to 608.78ms, raising the average scan processing time to 18.13ms. However, we believe that running the modeling and odometry tasks in parallel would remove any timing inconsistencies affecting real-time usage; which we leave as future work.

B. Results on Snail-Radar

In addition to NTU4DRadLM, we perform additional testing on the Snail-Radar dataset [32], which uses both Oculii Eagle and ARS548 radars together with an Xsens MTi-3-DK IMU, and includes sequences recorded in harsher environment conditions. In particular, we selected the five sequences recorded on 2023/12/13 because of the nighttime and rain conditions of that day under a high speed car platform. The longest tested sequence (`iaf_20231213_2`) is 15 min in length, while the others are around 7 min.

Table II shows results using the Oculii Eagle radar. In general, we can observe the best results to be spread across the different methods. Nonetheless, our Gaussian algorithms

obtain the best or second best results in 9 out of 10 metrics, and the best translation error in 3 out of 5 sequences (the other two favoring NDT). The multi-hypothesis approach improves or matches results compared to the single hypothesis version in 3 out of 5 sequences. We also note that NDT seems to behave much better in Snail-Radar than in NTU4DRadLM.

Table II also shows results using the ARS548 radar. This radar produces much sparser point clouds than Oculii Eagle (around 10x fewer points). We believe this to be the effect of Oculii Eagle’s scan enhancement algorithm. However, we can observe better metrics in general compared to Oculii Eagle. The sparser scans trigger a known issue in PCL’s implementation of NDT that cause a program termination, so unfortunately NDT is excluded from the comparison. The results once again show different methods leading in different sequences, however it is worth pointing out that 6 out of the 10 best results are now obtained by our Gaussian algorithms, as well as 3 out of the 10 second best results. Another thing to mention is that the multi-hypothesis scan matching seems to perform worse than the single-hypothesis version. We hypothesize this to be related to the increased sparsity of the scans, and believe it could be solved by improving the sampling distribution of the particles.

C. Additional qualitative experiments

In order to further justify our modeling approach based on globally optimized 3D Gaussians versus existing voxel-based approaches, we compare in Fig. 2 the output of our method against NDT. To do this, we prepare a radar-based map of NTU4DRadLM’s cp sequence using the supplied ground truth, and model a section of said map with both NDT and our method. The positions and sizes of the Gaussians generated by NDT are clearly constrained and influenced by the voxel grid, while our approach generates better fitted Gaussians. Moreover, our method is able to preserve geometric details such as corners, and allocates a higher budget of Gaussians to areas with higher point density, resulting in overall better representation of the geometry.

Additionally, we include a video supplement. In the video we show several Gaussian models of the same map created using different points-per-Gaussian ratios. It can be seen that, regardless of said hyperparameter, our modeling method is able to generate a representation reasonably fitting the map. Different number of Gaussians are allocated to areas of the map depending on the density and complexity of the area, as well as the available budget. Moreover, when the ratio is higher (meaning fewer Gaussians), sparse regions with few (outlier) radar points do not receive any Gaussians. Finally, we also include an example of the radar-inertial odometry pipeline on the same NTU4DRadLM cp sequence, compared to the ground truth trajectory.

D. Summary of results

We consider that the results above validate our methodology. Our Gaussian modeling and scan matching algorithm produces comparable relative translation and rotation metrics

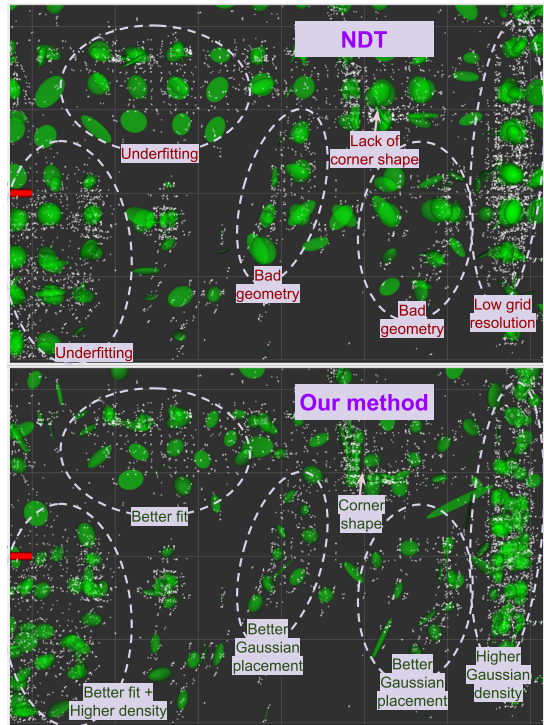


Fig. 2. Qualitative comparison between NDT and our Gaussian modeling using NTU4DRadLM’s cp sequence.

to existing registration algorithms, as shown by the experiments. Moreover, in several sequences across several datasets and radar types our algorithm produces the best overall results. On the other hand, the multi-hypothesis approach seems to need further adjustments, although it is already capable of producing better results for some sequences.

As an additional observation, it is worth mentioning that we believe the radar-to-IMU calibration file provided by NTU4DRadLM to be inaccurate, as it does not seem to match the placement of the different sensors in the photo they provide of their platform. The effects of this inaccurate calibration can be especially seen in the rotational errors, which are much higher for all methods compared to those achieved under Snail-Radar sequences.

VII. CONCLUSION

In this paper we introduce modeling and scan matching algorithms based on 3D Gaussians, which initialize and jointly optimize all parameters of a 3D Gaussian model to fit a radar point cloud, and make use of multiple hypothesis to support a scan matching process for subsequent incoming point clouds. Through experiments in multiple datasets with multiple radar types, we show that these methods produce results comparable to existing registration algorithms, and even manage to outperform them in several sequences. At the same time, our methods offer higher flexibility/expandability and faster scan matching compared to existing approaches based on individual points and voxelization [1] [2] [15] [16].

Future works include improving the run-time efficiency of the Gaussian modeling (replacing gradient descent, and run-

ning in parallel to the odometry pipeline), better initialization and dynamic management of Gaussians (as in 3DGS), as well as incorporating radar-specific information such as RCS (Radar Cross Section) values, and improving the robustness of the multi-hypothesis particle system with kinematic priors. Another line of work is further development of the RIO pipeline, using techniques such as Pose Graph Optimization (PGO), loop closure, and creating a global Gaussian map of the environment for the purposes of full SLAM.

ACKNOWLEDGMENT

This work was partially supported by the following grants: 1) INSERTION PID2021-127648OB-C31, and 2) NOR-DIC TED2021-132476B-I00 projects, funded by MCIN/AEI/10.13039/501100011033 and the “European Union NextGenerationEU / PRTR”.

REFERENCES

- [1] P. Biber and W. Strasser, “The normal distributions transform: a new approach to laser scan matching,” in *Proceedings 2003 IEEE/RSJ International Conference on Intelligent Robots and Systems (IROS 2003)* (Cat. No.03CH37453), vol. 3, 2003, pp. 2743–2748 vol.3.
- [2] A. Segal, D. Hähnel, and S. Thrun, “Generalized-ICP,” in *Robotics: Science and Systems*. The MIT Press, 2009.
- [3] J. Zhang and S. Singh, “LOAM: Lidar Odometry and Mapping in Real-time,” in *Robotics: Science and Systems*, 07 2014.
- [4] H. Wang, C. Wang, C. Chen, and L. Xie, “F-LOAM: Fast LiDAR Odometry and Mapping,” in *2021 IEEE/RSJ International Conference on Intelligent Robots and Systems (IROS)*, 2020.
- [5] P. Pfreundschuh, H. Oleynikova, C. Cadena, R. Siegwart, and O. Andersson, “COIN-LIO: Complementary Intensity-Augmented LiDAR Inertial Odometry,” in *2024 IEEE International Conference on Robotics and Automation (ICRA)*. IEEE, 2024, pp. 1730–1737.
- [6] B. Kerbl, G. Kopanas, T. Leimkühler, and G. Drettakis, “3D Gaussian Splatting for Real-Time Radiance Field Rendering,” *ACM Transactions on Graphics*, vol. 42, no. 4, July 2023. [Online]. Available: <https://repo-sam.inria.fr/fungraph/3d-gaussian-splatting/>
- [7] J. Zhang, R. Xiao, H. Li, Y. Liu, X. Suo, C. Hong, Z. Lin, and D. Wang, “4DRT-SLAM: Robust SLAM in Smoke Environments using 4D Radar and Thermal Camera based on Dense Deep Learnt Features,” in *2023 IEEE International Conference on Cybernetics and Intelligent Systems (CIS) and IEEE Conference on Robotics, Automation and Mechatronics (RAM)*, 2023, pp. 19–24.
- [8] J. Zhang, H. Zhuge, Y. Liu, G. Peng, Z. Wu, H. Zhang, Q. Lyu, H. Li, C. Zhao, D. Kircali, S. Mharolkar, X. Yang, S. Yi, Y. Wang, and D. Wang, “NTU4DRadLM: 4D Radar-Centric Multi-Modal Dataset for Localization and Mapping,” in *2023 IEEE 26th International Conference on Intelligent Transportation Systems (ITSC)*, 2023, pp. 4291–4296.
- [9] J. Zhang, H. Zhuge, Z. Wu, G. Peng, M. Wen, Y. Liu, and D. Wang, “4DRadarSLAM: A 4D Imaging Radar SLAM System for Large-scale Environments based on Pose Graph Optimization,” in *2023 IEEE International Conference on Robotics and Automation (ICRA)*, 2023, pp. 8333–8340.
- [10] X. Wu, Y. Chen, Z. Li, Z. Hong, and L. Hu, “EFEAR-4D: Ego-Velocity Filtering for Efficient and Accurate 4D radar Odometry,” 2024. [Online]. Available: <https://arxiv.org/abs/2405.09780>
- [11] D. Wang, S. May, and A. Nuechter, “RIV-SLAM: Radar-Inertial-Velocity optimization based graph SLAM,” in *2024 IEEE 20th International Conference on Automation Science and Engineering (CASE)*, 2024, pp. 774–781.
- [12] Y. Zhuang, B. Wang, J. Huai, and M. Li, “4D iRIOM: 4D Imaging Radar Inertial Odometry and Mapping,” *IEEE Robotics and Automation Letters*, vol. 8, no. 6, pp. 3246–3253, 2023.
- [13] P.-C. Kung, C.-C. Wang, and W.-C. Lin, “A Normal Distribution Transform-Based Radar Odometry Designed For Scanning and Automotive Radars,” in *2021 IEEE International Conference on Robotics and Automation (ICRA)*, 2021, pp. 14417–14423.
- [14] X. Li, H. Zhang, and W. Chen, “4D Radar-Based Pose Graph SLAM With Ego-Velocity Pre-Integration Factor,” *IEEE Robotics and Automation Letters*, vol. 8, no. 8, pp. 5124–5131, 2023.
- [15] K. Koide, M. Yokozuka, S. Oishi, and A. Banno, “Voxelized GICP for Fast and Accurate 3D Point Cloud Registration,” in *2021 IEEE International Conference on Robotics and Automation (ICRA)*, 2021, pp. 11 054–11 059.
- [16] Z. Qiao, Z. Yu, B. Jiang, H. Yin, and S. Shen, “G3reg: Pyramid graph-based global registration using gaussian ellipsoid model,” *IEEE Transactions on Automation Science and Engineering*, vol. 22, pp. 3416–3432, 2025.
- [17] B. Mildenhall, P. P. Srinivasan, M. Tancik, J. T. Barron, R. Ramamoorthi, and R. Ng, “NeRF: Representing Scenes as Neural Radiance Fields for View Synthesis,” in *ECCV*, 2020.
- [18] H. Matsuki, R. Murai, P. H. Kelly, and A. J. Davison, “Gaussian Splatting SLAM,” in *Proceedings of the IEEE/CVF Conference on Computer Vision and Pattern Recognition (CVPR)*, June 2024, pp. 18 039–18 048.
- [19] N. Keetha, J. Karhade, K. M. Jatavallabhula, G. Yang, S. Scherer, D. Ramanan, and J. Luiten, “SplaTAM: Splat Track & Map 3D Gaussians for Dense RGB-D SLAM,” in *Proceedings of the IEEE/CVF Conference on Computer Vision and Pattern Recognition (CVPR)*, June 2024, pp. 21 357–21 366.
- [20] Anonymous, “Gaussian-SLAM: Photo-realistic Dense SLAM with Gaussian Splatting,” *Submitted to Transactions on Machine Learning Research*, 2024, under review. [Online]. Available: <https://openreview.net/forum?id=sbkKi8snqH>
- [21] R. Xiao, W. Liu, Y. Chen, and L. Hu, “LiV-GS: LiDAR-Vision Integration for 3D Gaussian Splatting SLAM in Outdoor Environments,” *IEEE Robotics and Automation Letters*, vol. 10, no. 1, pp. 421–428, 2025.
- [22] S. Hong, C. Zheng, Y. Shen, C. Li, F. Zhang, T. Qin, and S. Shen, “GS-LIVO: Real-Time LiDAR, Inertial, and Visual Multisensor Fused Odometry With Gaussian Mapping,” *IEEE Transactions on Robotics*, vol. 41, pp. 4253–4268, 2025.
- [23] Y. Xie, Z. Huang, J. Wu, and J. Ma, “GS-LIVM: Real-Time Photo-Realistic LiDAR-Inertial-Visual Mapping with Gaussian Splatting,” 2024. [Online]. Available: <https://arxiv.org/abs/2410.17084>
- [24] J. Ortiz, A. Clegg, J. Dong, E. Sucar, D. Novotny, M. Zollhoefer, and M. Mukadam, “iSDF: Real-Time Neural Signed Distance Fields for Robot Perception,” in *Robotics: Science and Systems*, 2022.
- [25] Q. Chen, S. Yang, S. Du, T. Tang, P. Chen, and Y. Huo, “LiDAR-GS: Real-time LiDAR Re-Simulation using Gaussian Splatting,” *arXiv preprint arXiv:2410.05111*, 2024.
- [26] V. Spruyt, “A geometric interpretation of the covariance matrix,” May 2021, accessed: December 2024. [Online]. Available: <https://www.visiondummy.com/2014/04/geometric-interpretation-covariance-matrix/>
- [27] P.-E. Forssén, “Low and Medium Level Vision using Channel Representations,” Ph.D. dissertation, Linköping University, Sweden, SE-581 83 Linköping, Sweden, March 2004, appendix C, Dissertation No. 858, ISBN 91-7373-876-X.
- [28] J. Solà, “Quaternion kinematics for the error-state Kalman filter,” 2017. [Online]. Available: <https://arxiv.org/abs/1711.02508>
- [29] C. Doer and G. F. Trommer, “An EKF Based Approach to Radar Inertial Odometry,” in *2020 IEEE International Conference on Multi-sensor Fusion and Integration for Intelligent Systems (MFI)*, 2020, pp. 152–159.
- [30] J. Rehder, J. Nikolic, T. Schneider, T. Hinzmann, and R. Siegwart, “Extending kalibr: Calibrating the extrinsics of multiple IMUs and of individual axes,” in *2016 IEEE International Conference on Robotics and Automation (ICRA)*, 2016, pp. 4304–4311.
- [31] V. Kubelka, E. Fritz, and M. Magnusson, “Do we need scan-matching in radar odometry?” in *2024 IEEE International Conference on Robotics and Automation (ICRA)*, 2024, pp. 13 710–13 716.
- [32] J. Huai, B. Wang, Y. Zhuang, Y. Chen, Q. Li, and Y. Han, “SNAIL radar: A large-scale diverse benchmark for evaluating 4D-radar-based SLAM,” *The International Journal of Robotics Research*, vol. 0, no. 0, p. 02783649251329048, 0. [Online]. Available: <https://journals.sagepub.com/doi/abs/10.1177/02783649251329048>
- [33] M. Grupp, “evo: Python package for the evaluation of odometry and SLAM,” <https://github.com/MichaelGrupp/evo>, 2017.
- [34] K. Koide, “small_gicp: Efficient and parallel algorithms for point cloud registration,” *Journal of Open Source Software*, vol. 9, no. 100, p. 6948, Aug. 2024.